

Contents

2	1	Experimental results	2
3		<i>Diamond irradiation study</i>	
4	1.1	Measurement setup	3
5	1.1.1	Preamplifiers	3
6	1.1.2	Diamond samples	5
7	1.1.3	Readout devices	6
8	1.1.4	Setup for the efficiency study using β particles	6
9	1.1.5	Room temperature α -TCT setup	7
10	1.1.6	Cryogenic α -TCT setup	7
11	1.2	Charged particle pulses and spectra	9
12	1.2.1	Noise limitations	9
13	1.3	Radiation limitations	10
14	1.3.1	Quantifying radiation damage in diamonds	11
15	1.3.2	Long-term measurement stability	14
16	1.4	Temperature limitations	20
17	1.4.1	Temperature-variant α -TCT before irradiation	20
18	1.4.2	Temperature-variant α -TCT after irradiation	21
19	1.5	Conclusion	28

²⁰ **Chapter 1**

²¹ **Experimental results**

²² *Diamond irradiation study*

²³ This chapter contains the measurement results of data taken with diamond sensors.
²⁴ First the measurement setup is described (section 1.1). Then the measured particle
²⁵ spectra are shown in 1.2. This is followed by a study of effects of irradiation damage
²⁶ on the electrical signal of the diamond detector and its lifetime. The last section
²⁷ shows the results of the measurements of irradiated diamond samples at cryogenic
²⁸ temperatures. The aim of these studies is to find the operational limitations of dia-
²⁹ mond detectors for spectroscopy and tracking applications. The studies compare the
³⁰ experimentally acquired data with the theory from the previous chapter and define
³¹ limitations of the diamond detectors in terms of noise, radiation and temperature.

³² Diamond sensors are mainly used for two types of measurements: particle counting
³³ and spectroscopy. The first type of measurements depends on the sensor's efficiency –
³⁴ the ability to detect all or at least a known percentage of radiation quanta (particles
³⁵ or photons) that hit it. The energy of the radiation is not so important; what bears
³⁶ the information is the rate and the spatial distribution. Here the radiation does
³⁷ not necessarily stop in the bulk, but rather continues its way. In spectroscopy, on
³⁸ the other hand, the idea is that a particle stops within the sensor, depositing all
³⁹ its energy, which is then measured via the freed charge carriers. The aim of the
⁴⁰ experiments described in this chapter is to:

- ⁴¹ 1. Quantify the efficiency of the sCVD diamond in counting mode,
- ⁴² 2. Quantify the degradation of efficiency with respect to the received radiation
⁴³ dose,
- ⁴⁴ 3. Quantify the macroscopic effects on charge carrier behaviour with respect to
⁴⁵ the received radiation dose and
- ⁴⁶ 4. Define limitations for its use in spectroscopy.

⁴⁷ The results discussed here show that there are several limitations for using diamond as
⁴⁸ a measurement device. All of them need to be taken into account for the measurement

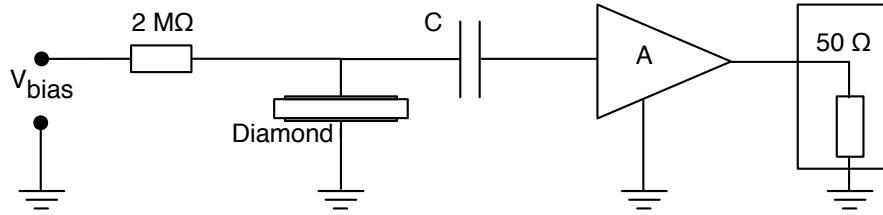


Figure 1.1: Diagram of a diamond detector readout chain.

device to perform reliably and stably. The first step is to build a setup that is insensitive to external electromagnetic interferences and minimises electrical noise in the system. The setup needs to be calibrated before use. Then, the measurement conditions have to be defined, such as the temperature, the type of radiation and its flux. This allows us to estimate the lifetime of the detector and predict the longterm change of the signal. This change can then be accounted for when interpreting the output data.

1.1 Measurement setup

To get reliable measurement results, great care has to go towards designing a measurement setup that minimises the noise in the measurements. Shielding has to be applied wherever possible. For instance, aluminium foil can be wrapped around the exposed parts of the system to shield them from external radio-frequency (RF) interferences. In addition, the sensors have to be covered to prevent the light from shining directly onto them. The incident photons can deposit enough energy to increase the leakage current of the detector.

The measurements using diamond that are explained in these chapters were carried out using several measurement setups, but they are all similar in terms of the electrical signal chain. The measurement chain consists of three main parts: a diamond sensor, a signal preamplifier and a readout device, as seen in diagram 1.1. The signals propagating along the analogue chain (before being digitised by the readout device) are fast – in the GHz bandwidth range – and with low amplitudes – of the order of tens of μV . This gives rise to importance of RF shielding. Also, the connection between the carrier and the preamplifier has to be as short as possible to avoid capacitive signal losses in the transmission line. Finally, the system needs to be grounded properly.

1.1.1 Preamplifiers

Two preamplifiers are used for the measurements, one sensitive to charge and the other to current. *CIVIDEC Cx* (figure 1.2a) is a charge sensing amplifier. Its high SNR (equivalent noise charge of $300 + 30 \text{ pF}^{-1} \text{ e}^-$ and a reported gain of $\sim 12 \text{ mV/fC}$) makes it a good choice for spectroscopic measurements with diamond

1.1. MEASUREMENT SETUP

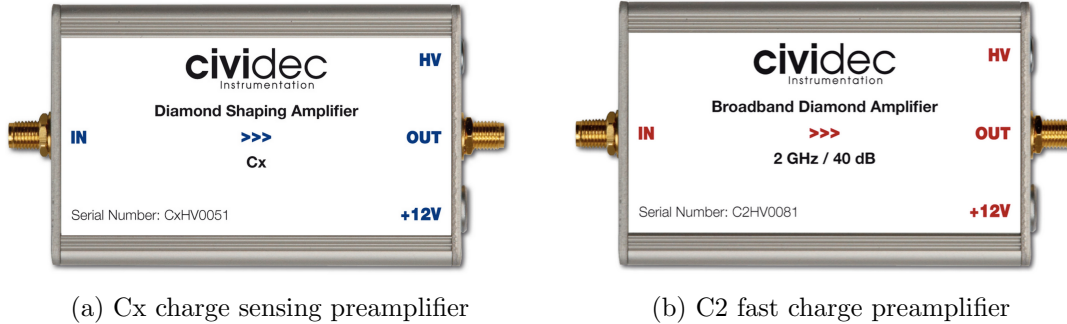


Figure 1.2: Amplifiers used for the charge and current measurements

78 sensors. *CIVIDEC C2* (figure 1.2b) is a fast current preamplifier with a 2 GHz band-
 79 width limit. It is used for TCT measurements because of its fast response and a good
 80 SNR. Both are embedded in an RF-tight aluminium box to reduce the noise pickup.
 81 Both have an AC coupled input and an output with a 50Ω termination.

82 Calibration

83 The amplifiers have to be calibrated before use to determine their gain. Both are
 84 calibrated using a square signal generator with a known amplitude step of $U_{\text{in}} =$
 85 (252 ± 5) mV. A 2 GHz oscilloscope with a 10 GS/s sampling is used to carry out
 86 these measurements.

87 In the case of the Cx charge sensitive amplifier, the signal is routed through a
 88 capacitor with a calibration capacitance $C_{\text{cal}} = (0.717 \pm 0.014)$ pF and then to the
 89 input of the amplifier. The pulse area behind the capacitor is $a_{\text{cal}} = (5.0 \pm 0.5)$ pVs,
 90 with the signal amplitude on the output amounting to $U_{\text{Cx}} = (1.95 \pm 0.05)$ V. The
 91 input voltage step combined with the calibration capacitance yields a calibration
 92 charge $Q_{\text{cal}} = C_{\text{cal}} \cdot U_{\text{in}} = (181 \pm 5)$ fC. The gain of the Cx amplifier is therefore
 93 $A_{\text{Cx}}^Q = \frac{U_{\text{Cx}}}{Q_{\text{cal}}} = (9.3 \pm 0.4)$ mV/fC or $A_{\text{Cx}}^a = \frac{U_{\text{Cx}}}{a_{\text{cal}}} = (390 \pm 40)$ mV/pVs. The area-based
 94 amplification factor has a higher uncertainty ($\sim 10\%$) than the amplitude-based
 95 factor ($\sim 4\%$) due to the measurement limitations of the oscilloscope. Nevertheless,
 96 it can be used as an estimate for the integrated charge of a current pulse.

97 To calibrate the C2 current amplifier, only the amplitude gain has to be measured.
 98 The input signal amplitude has to be such that it keeps the output amplitude within
 99 the amplifier's linear range, that is ± 1 V. The signal from the generator is therefore
 100 routed through a 36 dB attenuator to decrease its amplitude to $U_{\text{inAtt}} = (3.95 \pm$
 101 $0.05)$ mV. Two amplifiers with different gains have been measured, because both
 102 are used for the measurements at different times. The output of the first amplifier
 103 amounts to $U_{\text{C2-1}} = (860 \pm 5)$ mV. This yields the amplification gain equal to $A_{\text{C2-1}} =$
 104 $\frac{U_{\text{inAtt}}}{U_{\text{C2-1}}} = (217 \pm 3)$. The second amplifier has the output equal to $U_{\text{C2-2}} = (632 \pm 5)$ mV
 105 with the gain equal to $A_{\text{C2-2}} = (152 \pm 3)$.

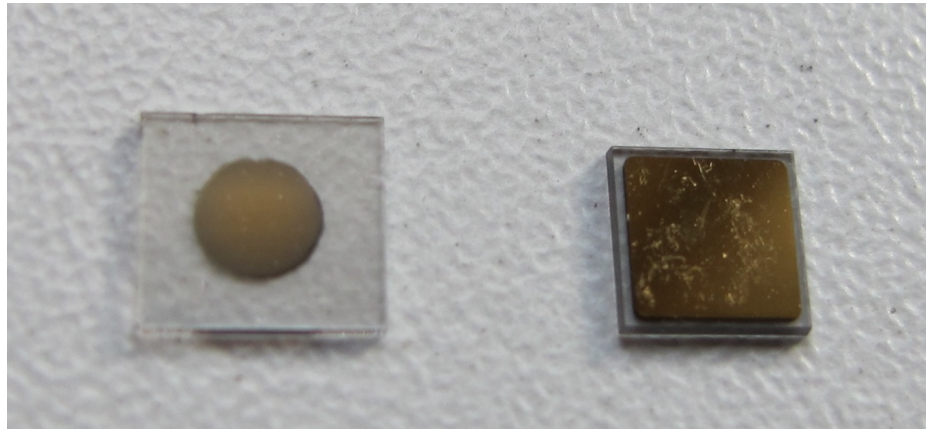


Figure 1.3: Two scCVD diamond samples: A IIa 1scdhq (left) and an E6 S37 (right)

1.1.2 Diamond samples

Detector-grade diamonds are very difficult to produce, mostly because it is very difficult to ensure a high enough purity of the lattice. The sensor samples used for these studies were bought at Element Six (E6) [1]. They all have the same standard dimensions. sCVD diamonds with dimensions $4.7 \times 4.7 \text{ mm}^2$ are already sufficiently large for most of the beam monitoring applications and still affordable. One of the samples with dimensions of $5.6 \times 5.3 \text{ mm}^2$ produced by IIa Singapore [2] was also sent to CERN to be characterised. The target thickness for all the samples is $500 \mu\text{m}$. Diamonds this thick yield a high enough signal-to-noise ratio for MIPs to be measured by the electronics. Table 1.1 shows all the samples used for this study. Two of them were later irradiated with 300 MeV pions and then compared to the pre-irradiated state. Irradiation doses for damaging the material need to be high – above 10^{12} particles per cm^2 to be able to observe change in the sensor's behaviour.

	Name	Type	Producer	Dimensions [mm^2]	Thickness [μm]	Electrode	Irradiated
	S37	sCVD	E6	4.7×4.7	548	Cr/Au	no
	S50	sCVD	E6	4.7×4.7	537	Cr/Au	no
	S52	sCVD	E6	4.7×4.7	515	Cr/Au	$1 \times 10^{14} \pi \text{ cm}^{-2}$
	S79	sCVD	E6	4.7×4.7	529	Cr/Au	$3.63 \times 10^{14} \pi \text{ cm}^{-2}$
	ELSC	sCVD	E6	4.7×4.7	491	Cr/Au	no
	1scdhq	sCVD	IIa	5.6×5.3	460	Cr/Au	no

Table 1.1: Diamond sensor samples used

The diamond samples have quoted impurity densities of $\leq 2 \times 10^{14} \text{ cm}^{-3}$ and nitrogen incorporation of $\leq 1 \text{ ppb}$. The electrodes were added by various companies and institutes. For instance, S52 was metallised by a company DDL [3] while the Physics Department of the University of Firenze, Italy metallised the S79. There are also several techniques for producing the electrodes. The DDL contacts consist of three layers: DLC (diamond-like carbon)/Pt/Au with 4/10/200 nm thicknesses, respectively. The metallisation for S79, on the other hand is made up of Cr/Au with

1.1. MEASUREMENT SETUP

a total thickness of \sim 400 nm. The area coverage also differs from sample to sample. Diamonds must not be metallised until the very edge as the proximity of contacts with a high potential can lead to sparking. However, the areas not covered by the metallisation are less efficient because the fringe fields at the edges are not as strong as in the middle. This effectively reduces the sensitive area of the sensors. In the diamonds used here the effective area was anywhere from 9 mm^2 to 18 mm^2 . Leakage current through the bulk was below 1 ns, but increased for the irradiated samples. The capacitance was of the order of $(2.0 \pm 0.3)\text{ pF}$.

1.1.3 Readout devices

Electrical signals in diamond detectors are in the GHz frequency range. To preserve this information, the readout device has to have a high bandwidth limit. For instance, a 250 MHz limit is enough for the spectroscopic measurements with the Cx charge amplifier, but might be insufficient for the current measurements with the C2 amplifier. Two devices are used take data shown in this chapter. The first choice is a 2 GHz LeCroy WaveRunner 204MXi-A. This specific model has a high enough limit for the fast current preamplifier signals. It offers a versatile solution for analogue signal readout – it is fast to set up and reliable. It is very convenient for use in lab tests and for experiments where small amounts of data are taken and where speed is not crucial. However, its slow acquisition speed turns out to be a bottleneck in the test beam experiment. Its initial 100 Hz readout rate decreases to a mere 20 Hz within 20 minutes, because every single trigger is saved as a separate file and the Windows operating system is not capable of handling 10000+ files in a single directory easily. This is why it has been exchanged with a DRS4 [], an analogue readout device developed by PSI, Switzerland. This compact device is capable of recording up to four waveforms at a time at a steady rate of up to 500 Hz. Its 700 MHz bandwidth limitation is sufficient for the signal from the charge amplifier.

1.1.4 Setup for the efficiency study using β particles

The efficiency study of the diamond sensors has been carried out at CERN in the North Hall test beam facility. There a straight high-energy particle beam of $\pi_{120\text{ GeV}}$ is provided to the users to calibrate their detectors. The beam had a transverse spread of $\sigma = 10\text{ mm}$ in both axes. The particle rate is of the order of $10^4\text{ }\pi\text{ cm}^{-2}\text{ s}^{-1}$. A diamond sensor embedded in a PCB carrier has been placed in the beam spot perpendicular to the beam and connected via an SMA connector directly to a charge amplifier (described below). The amplified signal is read out using a LeCroy oscilloscope and a DRS4 analogue readout system (both described below). A computer is used as a controller and data storage for the readout device. A beam telescope [] is used as a reference detector. It is a device that helps to cross-check the measurements of the devices under test (DUTs) and to carry out spatially resolved studies on the DUTs. It consists of several pixellated sensor planes placed in series, which can track a particle's trajectory with a precision of a few μm . The sensor planes are positioned

in front of the DUT and behind it. Then the beam telescope acts as a trigger system – it triggers the readout of both the telescope data and DUT data when both the planes in front and behind the DUT recorded a hit by the impinging particle. A particle detected by all the planes within the DUT window and the DUT itself counts towards its efficiency whereas a hit missed by the DUT means that the DUT is not 100 % efficient. To discard the hits that miss the DUT completely, a region of interest (ROI) can be chosen in the beam telescope planes. The equation for calculating the sensor efficiency is therefore

$$\epsilon = \frac{N_{\text{DUT}} \wedge N_{\text{telescope}}}{N_{\text{telescope}}} \quad (1.1)$$

for an ROI smaller than the sensitive region of the diamond.

1.1.5 Room temperature α -TCT setup

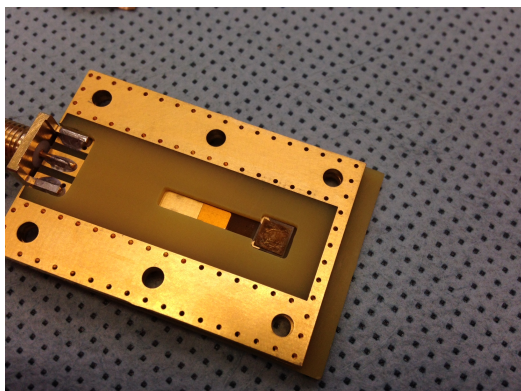
This TCT study is a follow-up of an extensive diamond TCT study at cryogenic temperatures []. The room-temperature TCT measurements have been carried out in the lab. The setup consists of a diamond sensor embedded in a PCB carrier, a current amplifier and an oscilloscope. To measure α particles, their energy loss during their trajectory has to be minimised. Therefore the diamond is placed inside a vacuum chamber. The chamber is a steel tube with a diameter of 5 cm. On one side it is connected to a vacuum pump via a steel pipe. A feedthrough with an SMA connector is placed on the other side. A C2 current amplifier is connected directly onto the feedthrough. The amplified output is connected to the oscilloscope via an SMA cable. An ^{241}Am source with a diameter of 2 cm and a height of 0.5 cm is fixed onto the sensor carrier (figure 1.4a, figure 1.4b). Then the carrier is inserted in the chamber and fixed in place using an air-tight clamp. The pump can then be switched on. It is capable of providing the inside pressure as low as 10^{-4} mbar after approximately one hour of operation, but measurements can take place even after five minutes of evacuation, at around 10^{-3} mbar. The most important thing to bear in mind is to switch the bias voltage of the sensor OFF during the process of evacuation, because the gas becomes more conductive at the pressure of the order of 10^{-1} mbar []. A failure to switch off the bias voltage may cause a spark between the signal and ground line, destroying the amplifier.

1.1.6 Cryogenic α -TCT setup

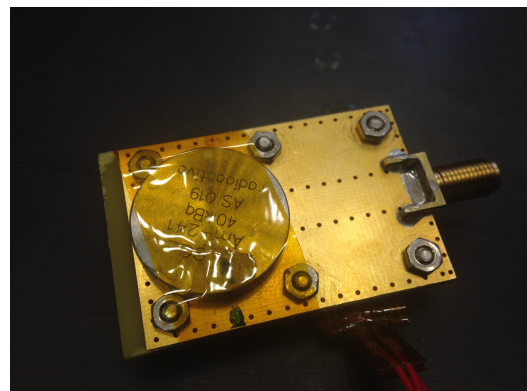
The experiment at cryogenic temperatures has been carried out in the cryolab at CERN. The room-temperature TCT setup has to be modified to allow for measurements at temperatures as low as 2 K. It consists of three parts:

- 202 1. a cryostat – a thermally insulated cylinder capable of containing liquid helium,
- 203 2. an inlet – an air-tight mechanical tube with valves and feedthroughs at the top
204 that is lowered in the liquid helium and

1.1. MEASUREMENT SETUP



(a) PCB carrier with an embedded diamond sample



(b) Radioactive source over the carrier

Figure 1.4: Positioning of the α -source on top of the sensor carrier

- 205 3. the diamond sample embedded in a PCB carrier with a fitted temperature
206 sensor, a heater and cables leading to the feedthroughs.

207 The setup is described in detail in [1].

208 When the diamond sample is placed in the PCB carrier and the ^{241}Am source is in
209 place, the inlet is sealed and lowered in the empty cryostat. Then the inside volume
210 of the inlet is evacuated to down to 10^{-5} mbar while the liquid helium is flowing into
211 the cryostat. To improve the thermal contact between the diamond and the coolant,
212 a small amount of helium gas is added inside the evacuated inlet, setting the vacuum
213 to around 10^{-3} mbar. This value changes with time, because the gas condenses on
214 the walls of the inlet, reducing the number of floating particles. For this reason the
215 helium gas has to be added on an irregular basis. Every addition causes a significant
216 undershoot of the sample temperature, which had to be corrected for using a heater
217 placed on the back of the PCB carrier. Also, the added gas deteriorates the vacuum
218 inside the inlet. It is very important to monitor the pressure so as not to let it rise
219 above 10^{-2} mbar. The gas at this pressure is significantly more conductive and could
220 cause a short circuit between the two diamond plates or in the SMA connectors,
221 destroying the amplifier. Furthermore, at approximately 60 K the helium gas has to
222 be evacuated from the inlet to avoid a potential explosion due to the expansion of
223 the gas with temperature.

224 When the sample is cooled to the minimum temperature achievable by means
225 of liquid helium without over-pressurising it (4.2 K), the measurements start. A
226 temperature sensor placed on the back of the PCB carrier is used to measure the
227 temperature of the sample. After every temperature data point, the current through
228 the heater placed in the PCB next to the diamond sample is increased, warming up
229 the sample. The initial temperature time constant of the order of tenths of seconds at
230 low temperatures increases with temperature. Even more so when helium is evacuated
231 from the inlet at 60 K, removing the thermal bridge between the wall of the inlet and
232 the diamond sample. At the room temperature (RT), the time constant increases to

233 the order of minutes.

234 1.2 Charged particle pulses and spectra

235 In previous chapter the ionisation profiles for different types of radiation were dis-
236 cussed. It is known that β and γ radiation induces a triangular electric pulse whereas
237 α radiation induces a rectangular one. However, their amplitude, width and rise/fall
238 time depend heavily on the type of interaction with the diamond, the purity of the
239 diamond and the bandwidth of the amplifier and the oscilloscope. This section shows
240 the signal pulses of α , β and γ radiation with their respective energy distributions for
241 the case of a diamond detector. Then follows a discussion of effects of noise on these
242 measurements.

243 A CIVIDEC C2 current amplifier together with the LeCroy oscilloscope (both
244 with a bandwidth limit of 2 GHz) has been used to record the pulse shapes whereas
245 the Cx charge amplifier is used for charge measurement. A 2 GHz bandwidth limit
246 defines the minimum rising time equal to $t_r \simeq \frac{0.34}{BW} = \frac{0.34}{2 \times 10^9} = 170$ ps, therefore
247 the system is capable of measuring pulses with a minimum FWHM $\simeq 170$ ps. This
248 already makes it impossible to measure the initial peak in the α response due to the
249 two flavours of charge carriers travelling. If a charge carrier travelling through the
250 bulk takes $t_{t1} \sim 6$ ns to get to the electrode on the other side ($d_1 \sim 500$ μm), the
251 carrier with the opposite charge and a shorter path to the closer electrode – max.
252 $d_2 \sim 10$ μm – only takes $t_{t2} \sim \frac{d_2}{d_1} t_{t1} = 120$ ps. A drift time this short induces a
253 current pulse that is too narrow for the C2 amplifier or the oscilloscope to be able to
254 observe.

255 Figure 1.5 shows a set of pulses and an averaged pulse for α , β and γ radiation
256 using an ^{241}Am , ^{90}Sr and ^{60}Co source, respectively. The particles are measured with
257 the non-irradiated sCVD diamond S37. α particles always produce the same signal
258 pulse, but with a high noise RMS. The averaging suppresses the noise while still
259 retaining most the information. It does, however, smear the rising and falling edge,
260 increasing the rise time. The t_r is now of the order of 0.5 ns. Both β and γ pulses
261 look similar - triangular and with a wide range of amplitudes. Here the pulse count
262 is low, so the pulses with a high amplitude are not recorded. A trigger set very high
263 would be needed to “catch” them with the oscilloscope.

264 1.2.1 Noise limitations

265 Noise is a major limiting factor in particle detection. It defines the minimum measur-
266 able particle energy and the minimum measurement resolution. It is hence important
267 to minimise the electric noise in the detector signal. The major noise contribution
268 comes from poor shielding from external electromagnetic sources. These often cause
269 ringing, whereby the signal oscillates with a frequency defined by the external source.
270 The ringing makes high-frequency measurements impossible. Another source of noise
271 is the sensor itself. In the case of silicon, natural light increases the number of ther-

1.3. RADIATION LIMITATIONS

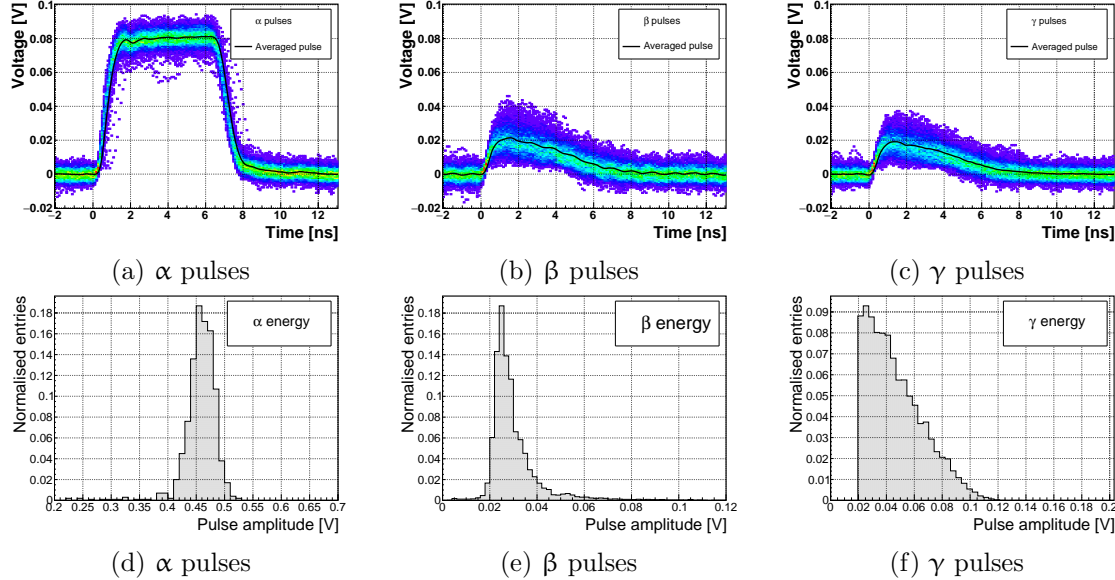


Figure 1.5: Superimposed and averaged pulses (a, b and c, current amplifier) and distributions of deposited energy (d, e, f, charge amplifier) for three types of radiation. Note the scale on the X axis of the distributions.

272 mally excited free charge carriers, increasing the leakage current. This is not the
 273 case for diamond, which is with its high energy band gap insensitive to visible light.
 274 Nevertheless, any noise produced by the sensors is amplified by the signal amplifiers,
 275 which add an additional noise of the analogue electrical circuit to the amplified
 276 signal. Finally, the digitisers add the quantisation noise to the digitised signal. If
 277 the measurement range is significantly higher than the actual measured signal, the
 278 quantisation noise can be a significant contributor to the decrease of the overall mea-
 279 surement resolution.

280 1.3 Radiation limitations

281 Exposure to ionising radiation degrades sensors. It introduces charge traps by damag-
 282 ing the sensor material. The electrons and holes created by the impinging particle get
 283 trapped in these traps, decreasing the induced current on the electrodes. This yields
 284 a lower integrated charge in an irradiated sensor than that in a non-irradiated one.
 285 Charge collection efficiency is therefore correlated with the level of irradiation. This
 286 section contains a study of the effects of pion ($\pi_{300 \text{ MeV}}$) irradiation on the charge col-
 287 lection efficiency of sCVD diamond detectors. To carry out this study, two diamond
 288 samples were irradiated to doses of $1 \times 10^{14} \pi \text{ cm}^{-2}$ (S79) and to $3.63 \times 10^{14} \pi \text{ cm}^{-2}$
 289 (S52). Then a test beam campaign was carried out to observe the charge collection
 290 efficiency at different bias voltage settings. The highest achieved efficiency values
 291 were used to determine the effective drop in efficiency with respect to received ra-
 292 diation dose. A model [] defined by a collaboration researching diamond behaviour

RD42 was applied to the measured values and a damage factor was extracted. The next subsection contains measurements and results of a long-term stability study using α and β particles. In particular, the charge collection efficiency as a function of time was measured during the measurements with β and α radiation. To investigate this effect on the scale of charge carriers, the change of TCT pulses with time was observed. Finally, a procedure that improves the pulse shape and with it the charge collection is proposed.

1.3.1 Quantifying radiation damage in diamonds

Radiation damage varies with the type of radiation (particles or photons) and its energy. There are several models existing [?, ?, ?] that try to explain the impact of irradiation and to provide *hardness factors* to compare the radiation damage between different particles. The standard way is to convert the damage into *neutron equivalent* []. Some models have been extensively verified with simulations and with experiments. In these experiments charge collection in sensors is measured before and after irradiation. This procedure is repeated several times, with a measurement point taken after every irradiation. When a set of measurements of charge collection is plotted against the radiation dose received by a specific particle at a specific energy, a damage factor k_λ can be extracted. Damage factors have to be measured across a range of energies and types of radiation to properly quantify the damage in the sensors []. They are then compared against the simulations to verify that the experimental observations are in line with the theory.

Diamond is an expensive material and the technology is relatively new as compared to silicon. Therefore not many institutes are carrying out diamond irradiation studies. To join the efforts, the RD42 collaboration [] was formed. It gathers the experimental results so far show no significant correlation with the NIEL (non-ionising energy loss) model [?], which correlates detector efficiency with the *number of lattice displacements*. Therefore an alternative model was proposed [?], correlating the diamond efficiency with *displacements per atom* (DPA) in the bulk. Figure 1.6 shows the DPA model for a range of energies of proton, pion and neutron irradiation in diamond. According to the figure, a 300 MeV pion beam damages the diamond bulk twice as much as a 24 GeV proton beam. The data points obtained by RD42 are also added to the figure. They have been normalised to damage by 24 GeV protons. Finally, the data point measured in the scope of this thesis has been added for comparison. The calculation is done below.

Irradiation with a $\pi_{300 \text{ MeV}}$ beam

The samples were irradiated at the Paul Scherrer Institute (PSI) [] by means of a beam of pions with an energy of 300 MeV (kinetic energy 191.31 MeV) and with a flux of up to $1.5 \times 10^{14} \pi \text{ cm}^{-2}$ per day. The system has a 10 % uncertainty on the beam energy. In addition, the equivalent fluence [] calculation has an error of $\pm 20 \%$.

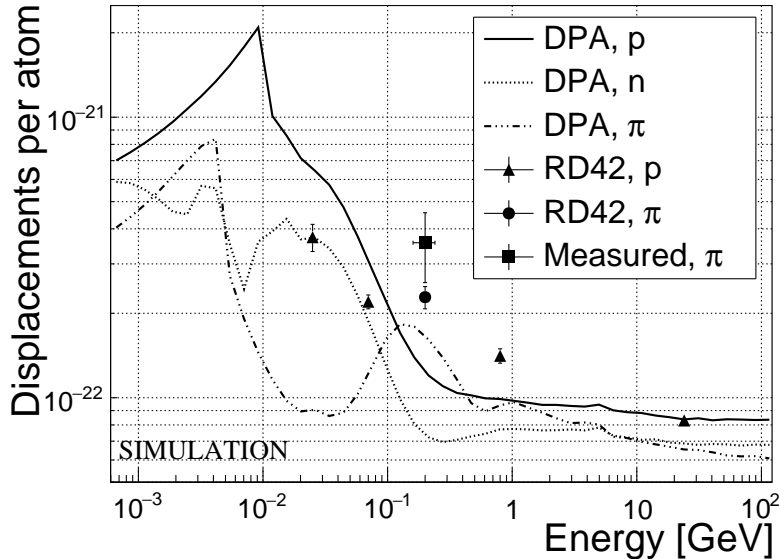


Figure 1.6: Diamond radiation damage - a model based on displacements per atom [1]. Added are data points for protons and pions by RD42 [2] and one data point for pions measured in the scope of this thesis.

333 Looking at the pion damage curve in figure 1.6, $\pi_{300 \text{ MeV}}$ point sits on a steep section
 334 of the DPA curve. This means that a deviation in beam energy can have a significant
 335 effect on the damage.

336 Two diamond samples, S52 and S79, were put in the $\pi_{300 \text{ MeV}}$ beam in the 2014
 337 PSI irradiation campaign; S52 to $(1 \pm 0.21) \times 10^{14} \pi \text{ cm}^{-2}$ and S79 to $(3.63 \pm 0.77) \times$
 338 $10^{14} \pi \text{ cm}^{-2}$. During the process, the golden electrodes got slightly activated, but the
 339 activation decayed in two weeks.

340 Charge collection efficiency and charge collection distance

341 Three diamonds – non-irradiated S37 and irradiated S52 and S79 – were tested in
 342 a $\pi_{120 \text{ GeV}}$ test beam [3] before and after irradiation. The goal was to estimate the
 343 charge collection efficiency (CCE) and charge collection distance (CCD) as a function
 344 of irradiation dose. The samples were primed (pumped) prior to data taking using a
 345 ^{90}Sr radioactive source. The data were then taken at a range of bias voltages ranging
 346 from 30 V to 900 V, yielding between $0.06 \text{ V}/\mu\text{m}$ and $1.8 \text{ V}/\mu\text{m}$ electrical field in
 347 the bulk. Every data point contained approximately 5×10^4 measured particles.
 348 The charge deposited by the particles was measured using a CIVIDEC Cx charge
 349 preamplifier. As expected, the integrated amplitude spectrum followed a landau
 350 distribution. Its most probable value (MPV) was used to calculate the most probable
 351 collected charge Q_i :

$$Q_i [e^-] = \frac{Q_i [fC]}{1.6 \times 10^{-4}} = \frac{MPV [mV]}{A [mV/fC]} \cdot 6.241 \times 10^4 \quad (1.2)$$

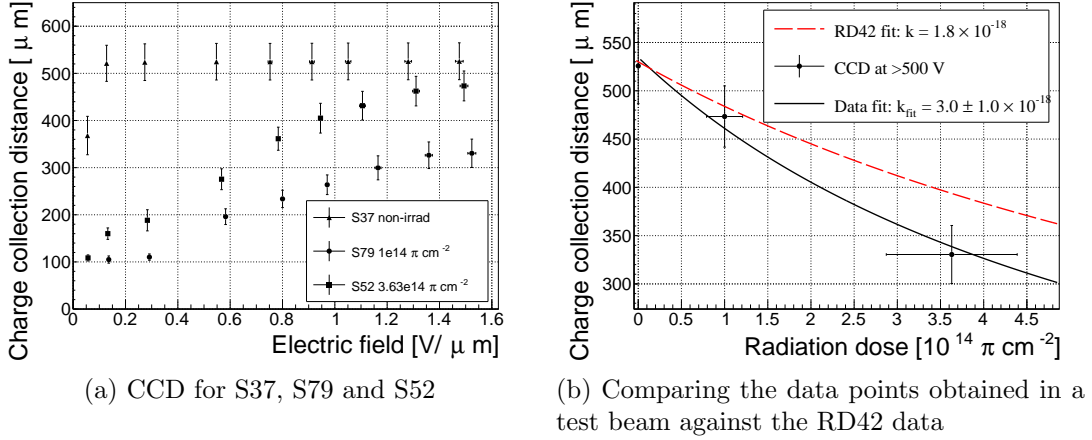


Figure 1.7: The charge collection distance at 500 V bias voltage for the three diamond samples was compared to the RD42 data for pion irradiation. The data points are about 5–15 % lower than expected from the RD42 data.

352 where $A = 9.2 \text{ mV/fC}$ is the preamplifier gain factor. The CCD was then calculated
 353 using the average number of electron-hole pairs produced per micrometer in diamond
 354 $\delta_d = 36 \text{ e-h } \mu\text{m}^{-1}$ (from table ??):

$$CCD = \frac{Q_i}{\delta d} \quad (1.3)$$

355 The resulting CCD for the three measured samples at bias voltages ranging from
 356 $0.2\text{--}1.6 \text{ V } \mu\text{m}^{-1}$ is shown in figure 1.7a. S37 exhibits full collection distance already
 357 at $0.4 \text{ V } \mu\text{m}^{-1}$ whereas the irradiated samples have a more gentle increase of CCD
 358 with increasing bias voltage. It is evident that at $1 \text{ V } \mu\text{m}^{-1}$ the maximum CCD has
 359 not been reached in the case of S79 and S52.

360 Irradiation damage factor

361 The irradiation damage factor k is a way to quantify irradiation damage of a specific
 362 particle at a specific energy. Via this factor different types of irradiation can be
 363 compared. It is obtained experimentally by measuring the CCD of a number of
 364 samples at various irradiation steps and fitting the equation 1.5 to the data. λ is the
 365 measured CCD, λ_0 is the CCD of a non-irradiated sample and Φ the radiation dose.

$$\frac{1}{\lambda} = \frac{1}{\lambda_0} + k_\lambda \cdot \Phi \quad (1.4)$$

$$\lambda = \frac{\lambda_0}{k_\lambda \lambda_0 \Phi + 1} \quad (1.5)$$

367 The data points with the maximum CCD obtained in the test beam measurements
 368 were plotted against radiation dose received (see figure 1.7b). Equation 1.5 was fitted
 369 to the data points and a damage factor $k_\lambda = (3.0 \pm 1.0) \times 10^{-18} \text{ } \mu\text{m}^{-1} \text{ cm}^{-2}$ was

1.3. RADIATION LIMITATIONS

370 obtained. This value is for a factor of two higher than the damage factor obtained by
371 RD42. A possible cause is that the irradiated samples did not yet have a full charge
372 collection at $1.5 \text{ V } \mu\text{m}^{-1}$. Also, with only two samples measured, the statistical
373 uncertainty was high. Nevertheless, it can be concluded that the 300 MeV pions
374 damage the diamond bulk more than the 24 GeV protons.

375 1.3.2 Long-term measurement stability

376 An important requirement for particle detectors is stable performance over long pe-
377 riods of time. For instance, the charge collection for a defined type and quantity of
378 radiation must not change over time or has to change in a predicted way. Diamonds
379 are stable as long as their environment and their operating point does not change
380 significantly. The stability of diamond detectors depends on many external factors.
381 The aim is to study the behaviour of diamond under controlled conditions, with the
382 goal to understand its limitations. One of these limitations is for sure the received
383 radiation dose. It might affect the long-term stability of the sensor during operation.

384 The three diamond samples (S37, S79 and S52) were exposed to two different types
385 of ionising radiation for a longer period to see if their behaviour changes over time.
386 Two parameters were observed in particular: 1) charge collection of β particles and
387 2) charge collection and ionisation profile of α particles. The results showed in both
388 cases that priming plays an important role in diamond measurement stability. The
389 β particles have a “healing” effect on the diamond; MIP detection is therefore rather
390 stable in the long run, despite the fact that the sensors had been degraded by means
391 of irradiation. Alpha particles, on the other hand, deteriorate the measurement,
392 probably by introducing space charge into the sensor bulk.

393 β long-term stability

394 The samples were intentionally not primed before the measurements took place. The
395 same initial conditions are usually found in HEP experiments. The measurement
396 setup consisted of a diamond sample with the Cx spectroscopic amplifier, a silicon
397 diode with a C6 amplifier for a trigger and a ^{90}Sr source on top. A particle emitted by
398 the source traversed the sensor bulk and hit the silicon diode, triggering the analogue
399 signal readout. The source was left on the top for the course of the experiment.
400 The measurements, however, took place at discrete times. For every data point,
401 approximately 10^4 triggers were recorded. The offline analysis of the recorded signal
402 pulse amplitudes yielded a landau distribution for every data point. The resulting
403 graph of charge collection over time (see figure 1.8) shows that the charge collection
404 efficiency improves over time when the diamond sensor is primed with a β source.
405 This is especially evident in the case of the two irradiated samples. S79 achieves close
406 to full efficiency whereas S52 reaches about 50 %. Both increases are significant.
407 After approximately 30 minutes the signal stabilises. As expected, the signal of the
408 non-irradiated S37 did not change with time – this pure sCVD diamond sample had
409 the maximum collection distance from the start.

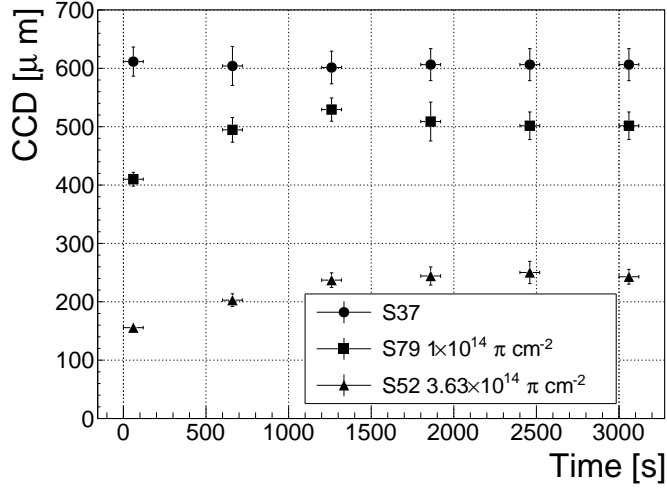


Figure 1.8: Increase of charge collection over time due to priming with the ^{90}Sr radioactive source

410 It should be noted that the ~ 2.28 MeV electrons emitted by this source are not
 411 MIPs; their charge deposition is higher than that of an electron MIP, according to
 412 the Bethe-Bloch distribution []. Nevertheless, for the purpose of these measurements
 413 this energy was adequate since only the relative change in charge collection was of
 414 our interest.

415 To sum up, diamond is a good choice for β radiation detection. Even if damaged by
 416 radiation, it reaches a stable charge collection in the order of an hour. The efficiency
 417 decreases with received radiation dose, but the decrease can be accounted for if the
 418 damage factor and the rate energy of the particles are known. γ radiation has a
 419 similar impact on the diamond as the β . The impinging photons, if they interact
 420 with the diamond, prime the bulk, causing the increase in charge collection efficiency.
 421 The difference, however, is in the interaction probability (cross section), which is
 422 several orders of magnitude lower for gammas.

423 α long-term stability

424 This part discusses the stability of irradiated diamond sensors during α measurements.
 425 It is safe to assume that they will behave differently than when subject to β radiation.
 426 This is due to the point-like charge carrier creation when an α particle impinges the
 427 bulk. The energy is approximately 20 times higher than the most probable value
 428 of a MIP; deposited in a small volume, it will behave differently to the track-like
 429 energy deposition of MIPs. In addition, carriers of only one polarity drift through
 430 the sensor while the others almost instantly recombine with the adjacent electrode.
 431 Taking into account that the diamond bulk has been damaged by irradiation, these
 432 two phenomena might have an effect on the operation of the detector on a macro
 433 scale.

1.3. RADIATION LIMITATIONS

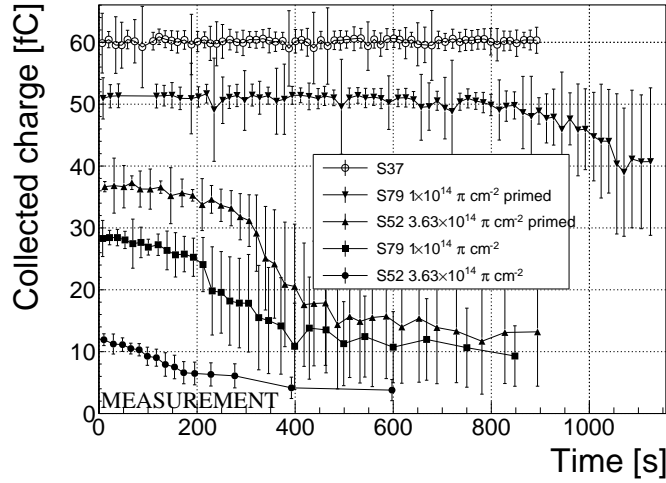


Figure 1.9: Comparison of collected charge with time for non-irradiated and irradiated diamond samples.

The measurement setup consisted of a PCB carrier for a diamond with a fitted ^{241}Am source and a vacuum chamber. The carrier was placed into the chamber, which was then evacuated. It acted as shielding for external noise pickup and ensured that the α particles didn't lose energy traveling through air. An SMA feedthrough ensured the electrical connection to the outside. The samples were measured before and after priming, at both polarities, to compare the behaviour of both electrons and holes as charge carriers. The scope of the measurements was to observe the changes in charge collection efficiency and/or in the pulse shapes.

The first test was carried out using the Cx spectroscopic amplifier. The bias voltage of the samples was set to +500 V and the signals from the diamond were measured for \sim 15 minutes. Figure 1.9 shows the results of these measurements. The collected charge for the non-irradiated sample was stable with time. It was expected that the irradiated samples will have a lower charge collection efficiency than the non-irradiated sample. However, their initial efficiency suddenly dropped after a certain period of time. The initial efficiency was improved after priming, but eventually it deteriorated again. In addition, the spread of measured energies increased significantly. Also, the particle counting rate decreased with the decreased efficiency.

The next step was to observe the behaviour of the current pulse shapes with time using a C2 current amplifier. The shape of the pulse holds more information about the charge carrier properties in the sensor than solely the value of the integrated charge. This time only the primed S79 sample was tested. Both hole and electron collection were observed to determine whether they behave differently or not. The sample was measured long enough for the pulse shapes to start changing. The data in figures 1.10 show that the initially stable pulses start deteriorating – suddenly there are several different shapes, some still the same as at the beginning while the others with almost zero amplitude. These data are difficult to interpret. Nevertheless,

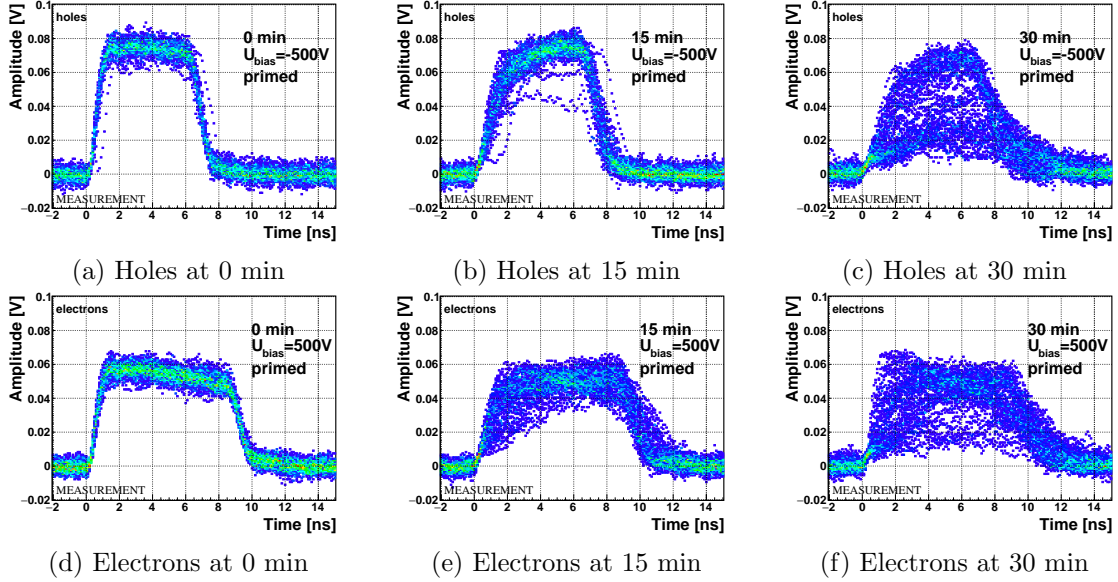


Figure 1.10: The signal of the irradiated and primed S79 deteriorates with time for both polarities. Every plot contains 60 superimposed pulses.

the idea is that some charges get trapped in the charge traps in the bulk for a long time, building up regions of space charge. Since only one charge flavour is drifting through the bulk whereas the other is quickly recombined, this already determines the imbalance in spatial distribution of trapped charges. The built up space charge affects the electric field, making it non-uniform. The non-uniform field in turn affects the drifting carriers, slowing them down or speeding them up, depending on the field gradient. Since the movement of the carriers is inducing the electric current, the field gradient can be observed in the signal. Unfortunately the effects are very convoluted, probably due to the entry point of the α particle.

At the beginning of every run, 60 reference pulses of the initial pulse were taken and plotted overlapped into a 2D histogram. An average pulse was extracted from this 2D distribution. Then a reference correlation between the reference pulses and the averaged pulse σ_{ref} was calculated. Subsequent data points also consisted of a set of 60 pulses. At every data point the correlation with the initial averaged pulse σ was calculated. From the ratio between the initial correlation σ_{ref} and discrete correlation values σ in time, the shape correlation $\text{Corr}_{\text{shape}}$ was calculated:

$$\text{Corr}_{\text{shape}}(t) = \frac{\sigma_{\text{ref}}}{\sigma} = \frac{\sum_x \sum_y w_{\text{ref}} \cdot (y_{\text{avg}} - y_{\text{ref}})^2}{\sum_x \sum_y w \cdot (y_{\text{avg}} - y)^2}, \quad (1.6)$$

where y_{avg} is the amplitude of the current averaged pulse at time x , y_{ref} is the amplitude of the initial averaged pulse at time x , y is the amplitude of the superimposed pulses in the 2D histogram and w and w_{ref} are weights for the superimposed pulses for the current data point and the initial data point.

Figure 1.11 shows the resulting time-resolved shape correlations. From the data obtained it can be concluded initial pulse shape quickly starts deteriorating. In fact,

1.3. RADIATION LIMITATIONS

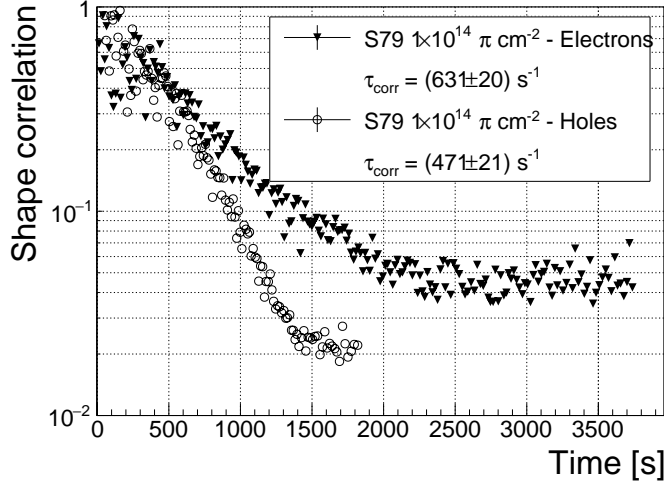


Figure 1.11: Deterioration of the pulse correlation with time

the deterioration of the shape correlation follows an exponential decay function, which was fitted to the data. The resulting decay constants for electrons and holes are $\tau_{\text{corr}_e} = (631 \pm 20) \text{ ns}^{-1}$ and $\tau_{\text{corr}_h} = (471 \pm 21) \text{ ns}^{-1}$. The electrons seem to retain the initial shape for longer. The deteriorated shapes also seem to be for a factor of 2 better than those of the holes.

Finally, an effort has made to find a way for the pulse shapes to return to their initial state. Five methods were tested:

1. Removing the source and leaving the bias voltage switched on,
2. Removing the source and switching the bias voltage off,
3. Priming with γ without bias voltage,
4. Priming with β with bias voltage switched on and
5. Priming with β without bias voltage.

The diamond sample S79 was first primed using a ^{90}Sr source for about one hour. Then the bias voltage was switched on and an ^{241}Am source was put on top. The pulses produced by the impinging α particles had a proper rectangular pulse at the beginning, but then started changing in an erratic way, as described in the text above. After approximately 30 minutes, one of the methods was tested. When a “healing” procedure was started, a set of 60 pulses was taken at irregular points of time to observe the change in the pulse shape and to assess the quality of the “healing” procedure. Then the bias voltage was switched off and the sample was primed again to reset its state before starting with the next run.

It turns out that the methods (3) and (5) improve the shape, method (2) helps slowly, (1) does not show any change with time and (4) at first improves, but then significantly degrades the shape. The effect observed in method (4) has already been

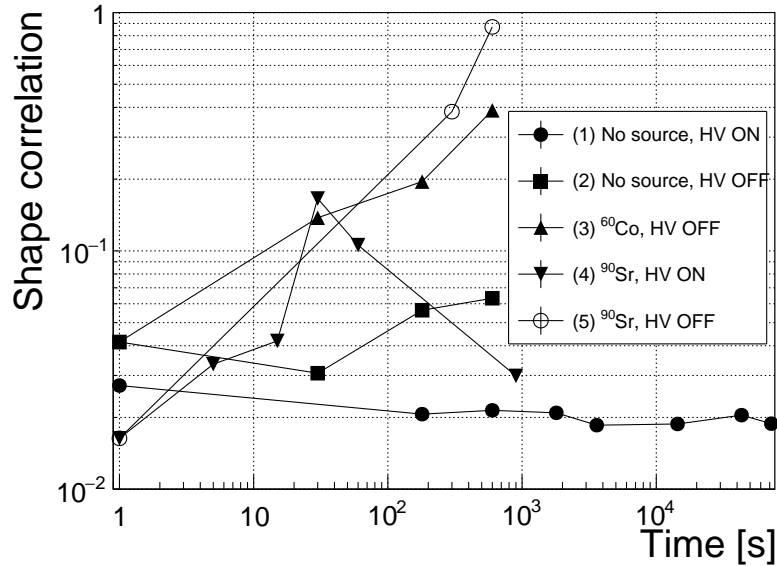


Figure 1.12: Five procedures of the “healing” process for an irradiated diamond that was exposed to α radiation at bias voltage switched on for at least 30 minutes.

described in [?]. The “healing” process therefore depends on the rate of radiation, the bias voltage and the time of exposure. The ionising radiation creates free charges, which quickly recombine close to the place of generation. It is likely that they also release the charges trapped during the measurement, reducing the overall effect of the space charge. The traps get filled with both flavours of carriers, thus they are neutralised. The pulse shape gradually returns to its initial state.

Procedure	Source	Bias voltage	Effectiveness
1	/	ON	no
2	/	/	slow
3	^{60}Co	/	YES
4	^{90}Sr	ON	no
5	^{90}Sr	/	YES

Table 1.2: Effectiveness of healing procedures

In summary, the shape of the pulses caused by α radiation changes with time for irradiated samples. The shape of the pulses gets distorted and becomes erratic. Charge collection decreases and its spread increases. This happens even faster for non-primed diamonds. To “heal” the diamond – to bring the pulse shapes back to their initial shape – the sample must be primed using a β or a γ source for several minutes at the bias voltage set to 0 V. Switching to the inverse polarity for a few seconds helps a bit, but in a long run distorts the signal, which cannot get back to its initial shape.

522 1.4 Temperature limitations

523 A test has been carried out to evaluate the effect of temperature changes on the
524 output signal of the diamond sensors. A cryostat filled with liquid helium is used to
525 cool down the sensor during the measurement process. The current signal response
526 to α -particles is measured at 18 temperature points between 4 K and 295 K. At every
527 temperature point, a set of 300 pulses is read out at various bias voltages. Resulting
528 data show that the charge collection is stable down to 150 K, where it starts decreasing
529 and stabilises again at about one third of the initial value at 75 K. This behaviour
530 was first measured and discussed by H. Jansen [?].

531 The band gap energy in diamond is equal to $E_g = 5.5$ eV while the average
532 energy to produce an electron-hole pair is $E_{e-h} = 13.25$ eV. This means there is
533 excessive energy deposited in the diamond bulk. The incident α -particle stops within
534 $\sim 10 \mu\text{m}$ of the bulk, transferring all its energy to the lattice. A part of this energy,
535 approximately 40 % [], directly ionises the carbon atoms, creating free electron-hole
536 pairs. The positively charged hole and the negatively charged electron in the hole
537 attract each other via the Coulomb force and may undergo a bonding process during
538 which a phonon is emitted.

539 The remaining energy, however, is converted into lattice vibrations (phonons [?]).
540 This means that the lattice within the ionisation volume (approximately $\sim 10 \mu\text{m} \times \sim 2 \text{ nm}$
541 in size) is briefly heated up. The hot plasma then cools down to the temperature of
542 the surrounding material by heat dissipation, (i.e. phonon transport). The free elec-
543 tron binds the free hole into a bound state (not recombination) – the exciton []. The
544 exciton binding energy is 80 meV. At higher temperatures, the lattice provides enough
545 energy to excite the electron from the exciton state back to the conduction band. At
546 lower temperatures, however, the exciton lifetime increases, which means that it will
547 take a longer time for the electrons to get re-excited to the conduction band. The
548 re-excitation lifetime at room temperature is ~ 30 ps, increasing to $\sim 150 \mu\text{s}$ at 50 K [].
549 This means that some of the bound electrons will not even start drifting within the
550 period of ~ 10 ns, which is the expected carrier drift time. When they are finally freed,
551 the current they induce is already hidden in the electronics noise. The effective area
552 of the observed current pulse is therefore smaller than that of a pulse induced by all
553 the carriers drifting at the same time. This in effect reduces the measured collected
554 charge. The longer the time constant, the lower the measured collected charge, as
555 shown in figure 1.17 below.

556 1.4.1 Temperature-variant α -TCT before irradiation

557 Three sCVD diamond samples have been tested at a range of temperatures using
558 the α -TCT technique. At each temperature point, the bias voltage is set to several
559 positive and negative values. A set of 300 pulses is recorded at every data point
560 and averaged offline. The resulting averaged pulses of sample S37 at the 260 K
561 temperature point and a bias voltage of ± 400 V, ± 500 V and ± 700 V are shown in
562 figure 1.13. The pulses induced by holes as charge carriers are shorter than those

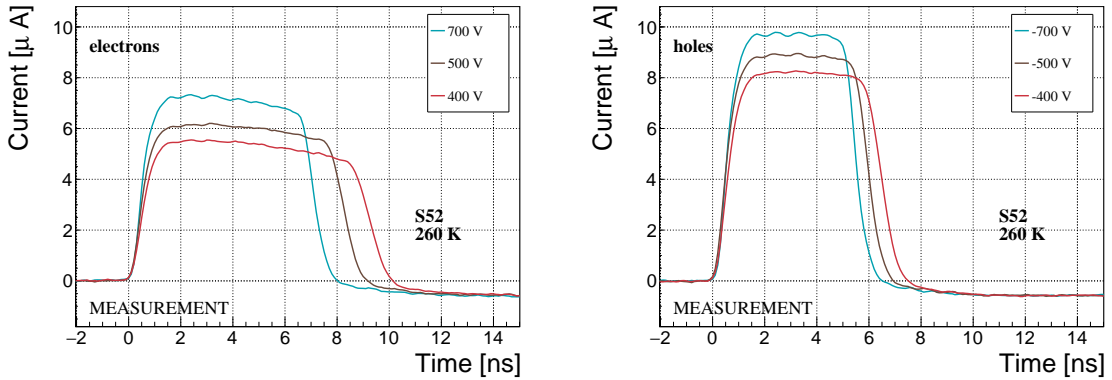


Figure 1.13: Varied bias voltage at a fixed temperature

induced by electrons, which means that holes travel faster in diamond. The area of the pulse, however, is the same for both polarities, which corresponds to the fact that the same amount of charges is drifting in both cases.

Figure 1.14 shows pulses at a bias voltage set to ± 500 V across the range of temperatures between 4 K and 295 K – room temperature (RT). Several conclusions can be drawn by observing their shape. First, the pulse shapes change with decreasing temperature. The pulse time gets shorter, hinting at the faster carrier drift velocity v_{drift} . Second, between 150 K and 75 K there is a significant change in shape - the time constant of the rising edge increases significantly and the pulse area decreases. From 75 K down to 4 K there is no significant observable change. Last, the top of the pulse at the S52 is not flat, which means that a portion of the drifting charge is lost along its way. This is due to charge trapping, likely by means of crystal defects or impurities.

1.4.2 Temperature-variant α -TCT after irradiation

The irradiated S79 and S52 have been re-tested in the cryostat after irradiation. The aim was to see how their pulse shapes change with decreasing temperature, in particular the decaying top of the pulses (see figure 1.15). The decay time gives information on trapping of charge carriers while travelling through the diamond bulk. A variation of the decay time constant as a function of temperature might help to reveal the type and depth of the charge traps. To observe these effects or lack thereof, a number of requirements has to be met. First, the diamond samples are intentionally not primed prior to the experiment because priming would improve the pulse shapes and possibly change the decay time constant of the signal. Second, keeping in mind that the pulse shape of irradiated diamonds changes with time, the duration of the measurement of an individual data point has to be short – of the order of 30 seconds. Last, the sequence of the bias voltage settings is important, the reason for which is explained below.

Unfortunately it is not possible to avoid temporal pulse changes. For instance,

1.4. TEMPERATURE LIMITATIONS

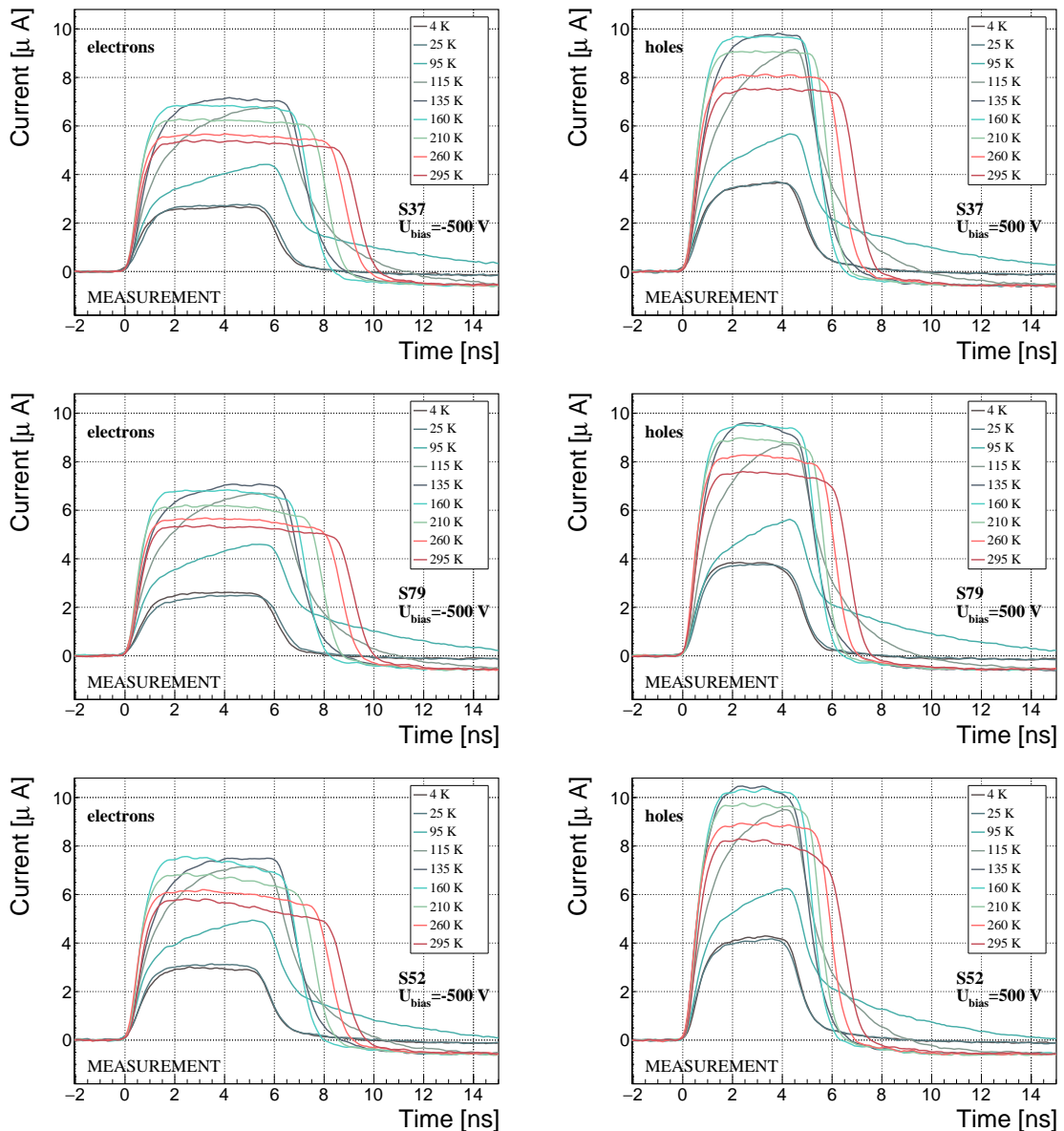


Figure 1.14: Several data points between 4 K and 295 K at a bias voltage of ± 500 V

one measurement point takes approximately one minute. After the measurement, the bias voltage polarity is swapped for a few seconds to bring the diamond back into its initial state. But a few seconds with respect to a minute is not enough. Therefore, when the bias voltage is set to the next value, there is still some residual effect of the previous measurement. Similar to the effects of polarisation, this effect is also decreasing the pulse height. This can be observed in figure 1.15, which shows the resulting pulses of S52 for bias voltages of ± 200 V, ± 300 V, ± 400 V and ± 500 V at 230 K and 260 K. In this case the measurements sequence is: 230K (200 V, 300 V, 400 V, 500 V, -500 V, -400 V, -300 V), 260 K (-200 V, -300 V, -400 V, -500 V, 500 V, 400 V, 300 V). The changes in pulse shapes for holes at 230 K and 260 K cannot be attributed to the temperature change. Instead, the explanation could lie in diamond “polarisation”. This means that, when exposed to an electric field with α measurements ongoing, the diamond builds up an internal electric field of inverse polarity, which effectively reduces the overall electric field. This internal field does not dissipate when the external bias voltage is switched off. It can be said that the diamond becomes “polarised”. When switching the polarity of the external bias voltage, the internal and external electric field point in the same direction at the beginning, increasing the overall electric field and with it the pulse height. In figure 1.15, this happens when switching from 500 V (figure 1.15a) to -500 V (figure ??) at 230 K. The built up polarisation contributes to the pulse having a sharp rising edge and a high amplitude. This effect decays during the next two voltage points. There would be a handful of ways to avoid this polarisation effect in the data:

1. After every data point invert the bias voltage and leave it to return to a neutral state for the same amount of time,
2. Make a hysteresis of data points, going from minimum negative to maximum positive bias several times,
3. Reduce the measurement time at every bias voltage setting.

Unfortunately, options (1) and (2) are very time consuming and would increase the overall experiment time to over one day. The third option would worsen the resulting averaged pulses. In the end an alternative option was chosen: alternating the starting bias voltage and the sequence at every temperature point. With this option, a meaningful systematic error in analysing the pulse shapes can be attained.

Figure 1.16 shows the irradiated S52 and S79 as well as the non-irradiated S37 for comparison, all at a bias voltage of ± 500 V and at several temperature points between 4 K and RT. It is evident that the radiation damage affected the shape of the pulses across all temperatures.

628 Collected charge as a function of temperature

629 The area below the current pulse is proportional to the charge collected by the dia-
630 mond detector. The collected charge is observed as a function of temperature. First,

1.4. TEMPERATURE LIMITATIONS

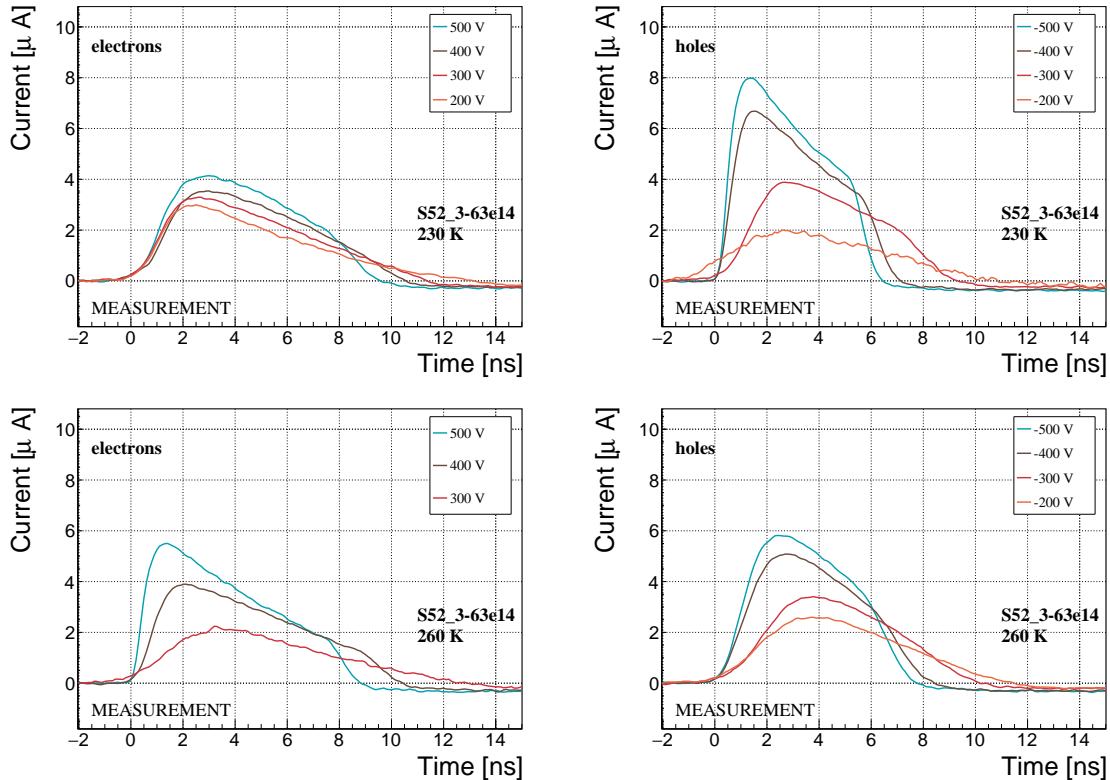


Figure 1.15: Varied bias voltage at a fixed temperature for an irradiated sample

the amplitude values of the averaged pulses at a bias voltage of ± 500 V and across the temperature range between 4 K and 295 K have to be integrated. Then a calibration factor is used to derive the charge for all data points. This factor is obtained using a Cx charge-sensitive amplifier. The resulting values for electrons and holes are plotted in figures 1.17a and 1.17b, respectively. Thesis [] gives a model that explains the drop in charge below 150 K. The new contribution are the data points for the irradiated samples. The values for them are lower than those of non-irradiated samples, which is expected.

The values for all samples are fairly stable in the range between 4 K and 75 K and between 150 K and 295 K. However, in the values for the irradiated S52 some excursions can be observed. This is due to the sequence of the measurement steps, which introduced a hysteresis effect and is explained in the preceding text.

The collected charge drops significantly from 150 K down to 75 K. In the non-irradiated samples the values in the lower temperature range are approximately 0.30 of the values at the high range. For the irradiated ones this difference is lower – a factor of 0.35 for S79 and 0.5 for S52. An interesting detail is that the ratio between the values for non-irradiated samples and their irradiated counterparts at the lower range is different than at the higher range. Looking at the values for the electron collection in figure 1.17a: for S52 the lower ratio is equal to 1.28 and the higher equal to 1.7. For S79 these ratios are 1.00 and 1.09, which means that the difference in

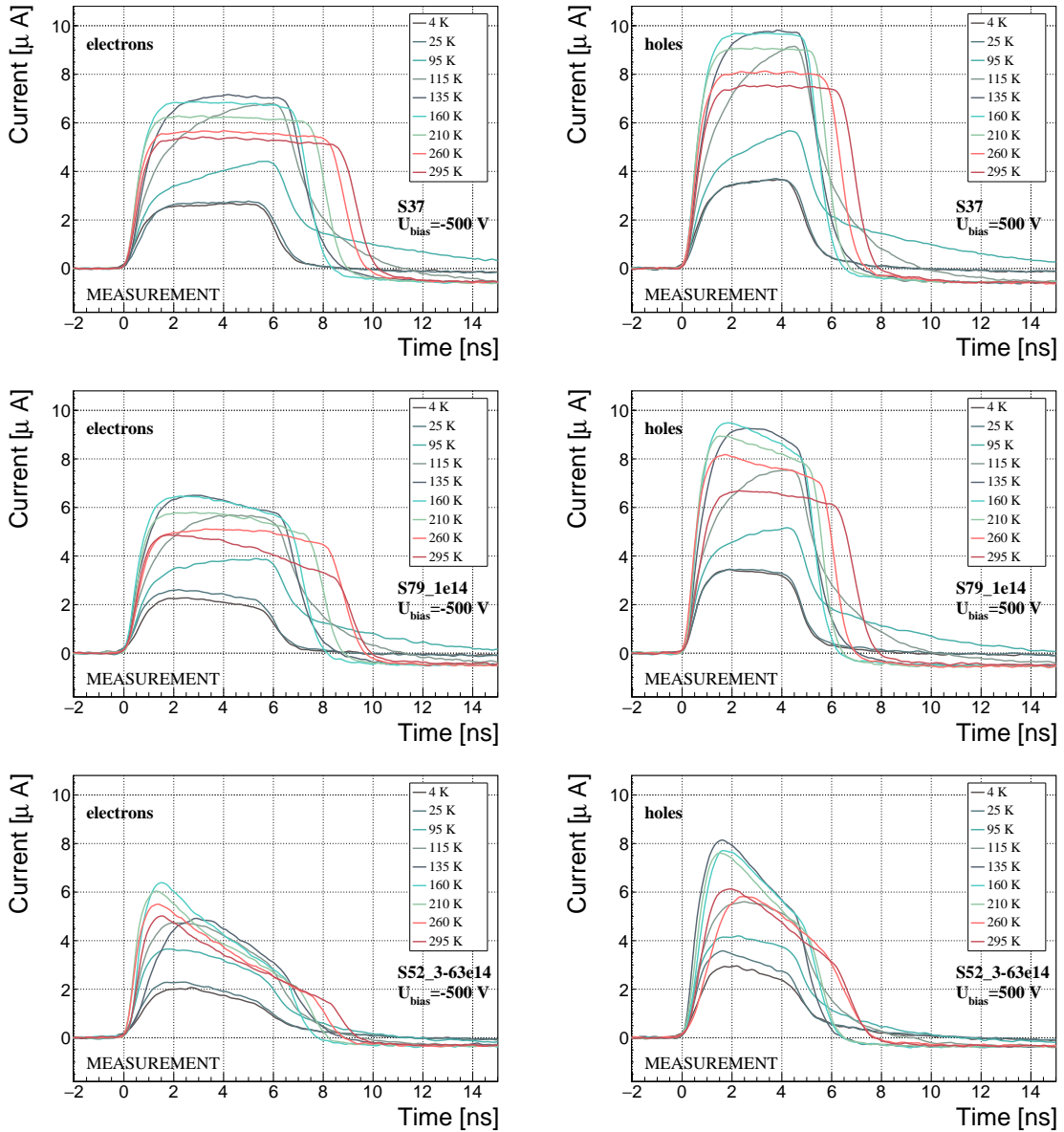


Figure 1.16: After irradiation: several data points between 4 K and 295 K at a bias voltage of ± 500 V

651 charge collection between 4 K and 75 K before and after irradiation is negligible.

652 Charge trapping

653 A decaying exponential function has been fitted to the decaying top of the averaged
654 pulses at bias voltages of ± 400 V and ± 500 V across all temperatures excluding the
655 transitional range between 75 K and 150 K. The resulting decay time constants τ
656 for an individual temperature point are not equal, which stems from the fact that
657 the pulses change with time due to “polarisation”. This counts as a systematic error.

1.4. TEMPERATURE LIMITATIONS

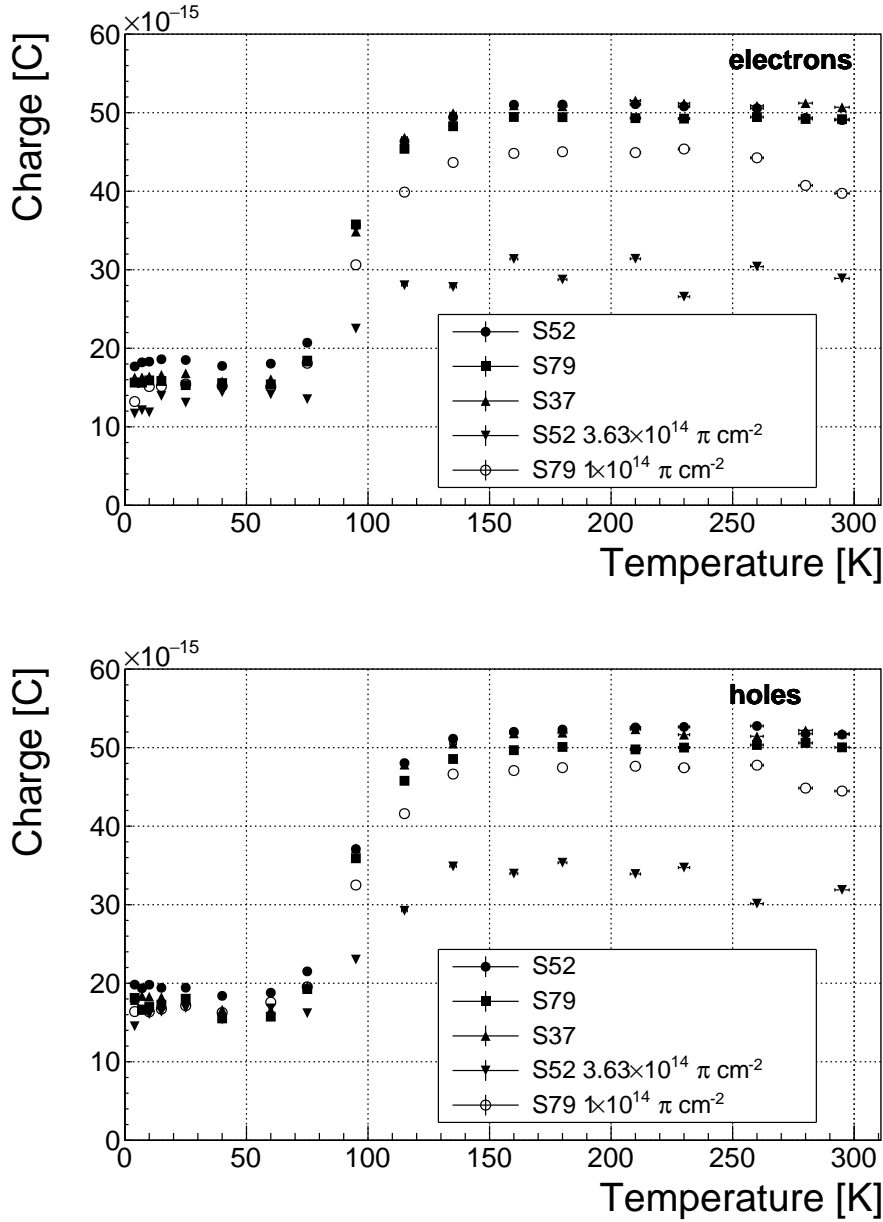
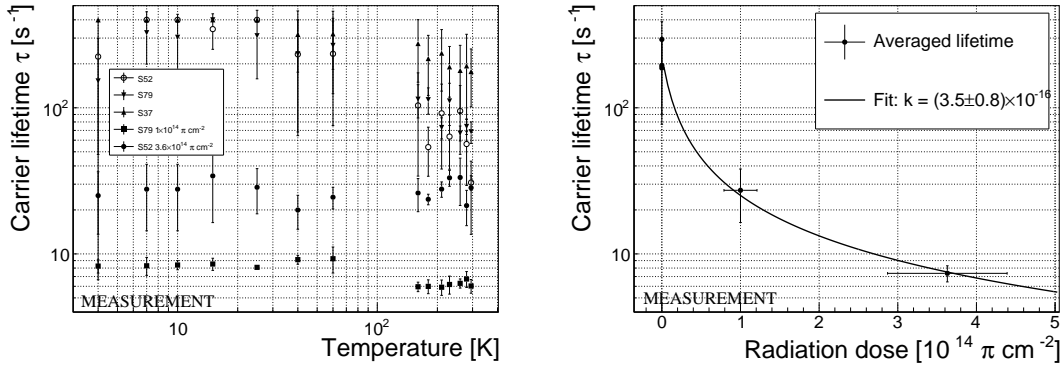


Figure 1.17: Collected charge as a function of temperature

658 Therefore the fitted τ for ± 400 V and ± 500 V are averaged into one value representing
 659 the measurement at that temperature point. Figure 1.18a shows the fitted τ for the
 660 five samples between 4 K and 295 K. In principle, the time constants should be infinite
 661 for a perfect and non-irradiated sample. Here a slightly tilted top of the pulse due to
 662 space charge is already successfully fitted with an exponential function, resulting in
 663 a τ of the order of (200 ± 20) ns⁻¹. Consequently the fitting method is not adequate
 664 for non-irradiated samples. For the irradiated samples, the fit becomes increasingly
 665 more meaningful. As seen in figure 1.18a, the fitted values of the irradiated samples



(a) Carrier lifetime as a function of temperature

(b) Carrier lifetime averaged over all temperatures as a function of π irradiation dose

Figure 1.18: Charge carrier lifetime decreases with irradiation, but is stable across the range of temperatures between 4 K – 75 K and 150 K – 295 K.

666 are fairly stable across all temperatures. There is a slight increase in the decay time
667 constant of the S52 from (6.0 ± 0.5) ns⁻¹ above 150 K to (8.5 ± 0.9) ns⁻¹ below 75 K.
668 On the other hand, this step is not observable in the S79 data. With only one sample
669 exhibiting this behaviour, the effect is not significant enough. Judging by the data
670 acquired, the samples would need to be irradiated to doses above $1 \times 10^{14} \pi \text{ cm}^{-2}$ to
671 quantify this effect in detail. So far this effect will not be regarded as significant for
672 the scope of this thesis. Building on this assumption, the conclusion is that the signal
673 decay time constant for irradiated sCVD diamond is constant across the temperature
674 range between 4 K and 195 K, excluding the transitional range between 75 K and
675 150 K.

676 Taking into account the conclusions above, all the values can be averaged into one
677 decay constant. Figure 1.18b shows these values for all samples as a function of the
678 received $\pi_{300 \text{ MeV}}$ radiation dose. To estimate the carrier lifetime with respect to the
679 radiation dose received, a similar model is used than that in section 1.5. This model
680 states that the inverse of the carrier lifetime is linearly decreasing with increasing
681 radiation dose:

$$\frac{1}{\tau} = \frac{1}{\tau_0} + \kappa_\tau \cdot \Phi \quad (1.7)$$

$$\tau = \frac{\tau_0}{\kappa_\tau \tau_0 \Phi + 1} \quad (1.8)$$

682 where τ_0 is the lifetime for a non-irradiated sample (real lifetime, therefore of the order
683 of 400 ns⁻¹), τ is the lifetime of an irradiated sample, Φ is the received radiation dose
684 and κ_τ the lifetime degradation factor. For these data the fitted factor is equal to
685 $\kappa_\tau = (3.6 \pm 0.8) \times 10^{-16} \text{ s cm}^2 \pi_{300 \text{ MeV}}^{-1}$. Using this factor, the steepness of the decay
686 in the pulse shape with respect to radiation dose can be estimated. This can help
687 when designing a system where current pulse shape is an important factor.

689 **1.5 Conclusion**

690 This chapter gives an overview of the capabilities and limitations of diamond as
691 a particle detector. Three effects on diamond were studied – noise, radiation and
692 temperature, the focus being on the latter two.

693 Two sCVD diamond detectors were irradiated with 300 MeV pions. They were
694 tested alongside a non-irradiated sample to observe the changes in the ability to detect
695 α , β and γ radiation. Their charge collection efficiency was measured in a test beam
696 facility using . The results were compared to the results from the RD42 collaboration
697 and a DPA model []. A radiation damage factor $k_\lambda = (3.0 \pm 1.0) \times 10^{-18} \mu\text{m}^{-1} \text{cm}^{-2}$
698 was obtained for $\pi_{300 \text{ MeV}}$ particles. The data point was not in agreement with the
699 data provided by RD42 nor with the model. However, the irradiation process and
700 the low number of tested samples hold a relatively high statistical uncertainty. In
701 addition, there was no diamond surface treatment done in between the measurements,
702 as is the case in the study conducted by RD42. The results obtained in the course
703 of these measurements will also be fed into the existing pool of data in the RD42
704 collaboration.

705 The next step was to test the long-term capabilities for α detection. The shape
706 of the ionisation profile was investigated to determine the behaviour of the charge
707 carriers in the irradiated diamond. An exponential decay was observed in the pulses
708 of irradiated samples, proving that there are charge traps in the bulk that were created
709 during irradiation. Then a long-term stability test was carried out. The results show
710 that the irradiated diamond detectors do not provide a stable and reliable long-term
711 measurement of α particles. This might be due to a space-charge build-up in the
712 bulk, which changes the electric field, affecting the charge carriers. A procedure to
713 improve the pulse shape using β and γ radiation was proposed.

714 Finally, the diamond sensors were cooled down to temperatures between 4 K and
715 295 K. Their response to α particles was observed. The results of the non-irradiated
716 and irradiated samples were compared. The effect of reduction for the number of
717 drifting charges due to exciton recombination was observed in both sets of data.
718 The second set had a superimposed effect of charge trapping during the drift, which
719 was represented by an exponential decay in the signal. The decay time constant
720 did not change with temperature. Therefore all temperature points for individual
721 samples were averaged and the decay time constants were plotted against the received
722 radiation dose. A damage factor equal to $\kappa_\tau = (3.6 \pm 0.8) \times 10^{-16} \text{ s cm}^2 \pi_{300 \text{ MeV}}^{-1}$ for
723 non-primed diamonds was defined.